Idealized Large-Eddy and Convection-Resolving Simulations of Moist Convection over Mountainous Terrain

DAVIDE PANOSETTI

Institute for Atmospheric and Climate Science, ETH Zürich, Zurich, Switzerland

STEVEN BÖING

Institute for Atmospheric and Climate Science, ETH Zürich, Zurich, Switzerland, and School of Earth and Environment, University of Leeds, Leeds, United Kingdom

LINDA SCHLEMMER

Institute for Atmospheric and Climate Science, ETH Zürich, Zurich, Switzerland

JÜRG SCHMIDLI

Institute for Atmospheric and Climate Science, ETH Zürich, Zurich, Switzerland, and Institute for Atmospheric and Environmental Sciences (IAU), Goethe University, Frankfurt, Germany

(Manuscript received 7 November 2015, in final form 1 July 2016)

ABSTRACT

On summertime fair-weather days, thermally driven wind systems play an important role in determining the initiation of convection and the occurrence of localized precipitation episodes over mountainous terrain. This study compares the mechanisms of convection initiation and precipitation development within a thermally driven flow over an idealized double-ridge system in large-eddy (LESs) and convection-resolving (CRM) simulations. First, LES at a horizontal grid spacing of 200 m is employed to analyze the developing circulations and associated clouds and precipitation. Second, CRM simulations at horizontal grid length of 1 km are conducted to evaluate the performance of a kilometer-scale model in reproducing the discussed mechanisms.

Mass convergence and a weaker inhibition over the two ridges flanking the valley combine with water vapor advection by upslope winds to initiate deep convection. In the CRM simulations, the spatial distribution of clouds and precipitation is generally well captured. However, if the mountains are high enough to force the thermally driven flow into an elevated mixed layer, the transition to deep convection occurs faster, precipitation is generated earlier, and surface rainfall rates are higher compared to the LES. Vertical turbulent fluxes remain largely unresolved in the CRM simulations and are underestimated by the model, leading to stronger upslope winds and increased horizontal moisture advection toward the mountain summits. The choice of the turbulence scheme and the employment of a shallow convection parameterization in the CRM simulations change the strength of the upslope winds, thereby influencing the simulated timing and intensity of convective precipitation.

1. Introduction

Moist convection is an important driver of day-to-day weather and is a major component of the water and energy cycles. It is thus essential to understand and accurately simulate it in both weather forecasting and climate prediction models. A large part of the inaccuracy of state-of-the-art numerical models in forecasting clouds and precipitation results from difficulties in simulating the triggering and the evolution of convective processes (e.g., Dai and Trenberth 2004; Brockhaus et al. 2008). One of the most relevant mechanisms initiating moist convection is the convergence of boundary layer (BL) air. Therefore, a successful simulation of convection initiation also

Corresponding author address: Davide Panosetti, Institute for Atmospheric and Climate Science, Universitätstrasse 16, ETH *Zürich*, CHN, CH-8092 Zurich, Switzerland.
E-mail: davide.panosetti@env.ethz.ch

DOI: 10.1175/JAS-D-15-0341.1

depends on a reasonable representation of BL processes (Petch et al. 2002).

Mountains of all scales can produce convergence at low levels and thus exert a strong local control on the formation of clouds and the rainfall distribution. The mechanisms leading to orographic convection and precipitation have been extensively reviewed in the literature (e.g., Banta 1984, 1990; Houze 1993). Among the prominent mechanisms are thermally induced wind systems. These wind systems determine the airmass exchange between mountainous regions and the adjacent plains and are observed on a wide range of scales, from the whole mountain range (e.g., Reiter and Tang 1984; Lugauer and Winkler 2005), to the scale of single valleys and slopes (e.g., Wagner 1932). Slope winds are an example of the latter category and are driven by horizontal density gradients generated by differential surface heating between the mountain peaks and the surrounding plains and valleys (e.g., Egger 1990; Whiteman 1990). On fair-weather days, slope winds are important for the transport and mixing of heat, moisture, and other constituents over mountainous terrain (Schmidli 2013). Convergence of upslope winds is an important convection initiation mechanism. Midlevel moistening associated with convective transport is narrowly focused over the mountain ridges (e.g., Orville 1968; Banta 1990; Damiani et al. 2008) and, if the wind is weak or absent, builds up for some time, leading to strong preconditioning and favoring the transition from shallow to deep convection (e.g., Kirshbaum 2011). Cloud organization (e.g., Kirshbaum and Grant 2012) and a supportive environment are also important contributing factors.

Recent enhancements in computing capacities have increasingly allowed for the running of convection-resolving numerical models [CRMs: often referred to as convection-permitting models in the literature; see, e.g., Prein et al. (2015)]. CRMs are mesoscale models with horizontal grid spacings of $O(1)$ km. Several studies have shown that even at grid spacings as large as 4 km deep convection can be successfully modeled without a convection parameterization scheme (e.g., Weisman et al. 1997; Hohenegger et al. 2008; Baldauf et al. 2011). The use of CRMs is motivated by previous encouraging results in both numerical weather prediction (e.g., Done et al. 2004; Lean et al. 2008; Schwartz et al. 2009) and regional-scale climate simulations (e.g., Hohenegger et al. 2008; Kendon et al. 2012; Ban et al. 2014). CRMs also appropriately represent the bulk feedbacks between moist convection and the larger-scale flow (Langhans et al. 2012b). However, despite large improvements in recent years, CRMs still have issues simulating both the spatial distribution and temporal evolution of precipitation (e.g., Xu et al. 2002; Bryan et al. 2003); this can in part result from their inability to represent shallow convection and from an inappropriate treatment of subgrid-scale turbulence.

The latter problem is well explained in Wyngaard (2004). Before computing resources allowed higher-resolution mesoscale modeling, there were two distinguished types of models: mesoscale models [$O(10)$ km mesh size], covering larger domains, and large-eddy simulation models [LESs; $O(100)$ m horizontal grid spacing], covering smaller domains in idealized studies. Their fundamental difference with regard to turbulence treatment is symbolized by the parameter $\alpha = l/\Delta$, where l is the energy-containing turbulence scale (1 km is a good order of magnitude for convective conditions), and Δ is the grid size. In mesoscale modeling, $\alpha \ll 1$, and therefore none of the turbulence can be resolved. In LES, on the other hand, the finer grid allows for explicit resolution of the largest BL eddies, and $\alpha \gg 1$. Turbulence in mesoscale models is often treated by simple one-dimensional (1D) turbulence schemes, which assume that the net effect of turbulence consists in a mostly vertical downgradient flux. In LES, three-dimensional (3D) subgrid-scale models are employed to account for the horizontal fluxes as well. However, in CRMs, the model resolution is roughly equal to the characteristic turbulence scales of convective structures ($\alpha \sim 1$; Craig and Dörnbrack 2008), and thus neither LES nor 1D turbulence schemes are strictly applicable. This is why this range of scales is called ''terra incognita'' (Wyngaard 2004) or the ''gray zone'' (e.g., Craig and Dörnbrack 2008).

Numerical simulations in the gray zone for BL turbulence not only have issues with turbulence treatment, but it is also questionable whether a shallow convection scheme should be employed. Most of the convection parameterization schemes employed in CRMs have in fact been devised for global climate models (e.g., Tiedtke 1989; Kain and Fritsch 1990) and are thus based on assumptions that are often violated at such horizontal grid spacing. Furthermore, in CRMs, the model grid size is roughly equal to or even larger than the typical horizontal size of shallow clouds. Therefore a shallow convection parameterization might still be necessary to capture sufficient moisture transport from the boundary layer into the midtroposphere.

In mountainous terrain, many problems with regard to turbulence and shallow convection parameterization in CRMs are accentuated. Most turbulence parameterization schemes assume horizontally homogeneous conditions and have been validated against observational data over flat terrain (e.g., Mellor and Yamada 1974, 1982; Rotach and Zardi 2007). This also affects the

performance of the convection parameterization scheme, in which the triggering and the closure often depend on turbulent processes in the subcloud layer (e.g., Kirshbaum 2011).

An LES at horizontal mesh spacing of $O(100)$ m is needed to explicitly resolve most of the underlying turbulent processes and can be used to address some of the CRM's deficiencies. Previous LES studies of orographic convection have focused on single hills or ridges (e.g., Kirshbaum 2011; Kirshbaum and Grant 2012) where, in the absence of a background flow, there is a strong preferential location for convective initiation at the mountain summit. A few recent idealized studies (e.g., Serafin and Zardi 2010; Schmidli and Rotunno 2010; Schmidli 2013; Wagner et al. 2014a,b) have examined the more complex case of a double mountain ridge, where the differential heating mechanisms between the valley atmosphere and the surroundings are crucial to determine where convective cells form. However, these studies only consider a dry atmosphere and thus do not account for any effect related to condensation, cloud cover, deep convection, and precipitation.

In this study, an analysis of the important processes for the initiation and subsequent development of moist convection and precipitation within a thermally driven flow is performed using LES modeling over idealized mountain ridges. A primary focus is on the role of moisture transport by the upslope winds and of vertical mixing. CRM simulations are also run to investigate the performance of a coarser-resolution model in reproducing the discussed mechanisms. In the CRM simulations, different turbulence schemes and a shallow convection parameterization are tested to understand if an optimal configuration exists to better match the LES results.

The numerical model and the experimental design are presented in section 2. In section 3, the methodology used to compute the water vapor budget and the subgrid-scale vertical fluxes of momentum is described. In section 4, the processes leading to convection initiation and precipitation development over a double mountain ridge are investigated using LES. Section 5 compares the LES with CRM simulations. The summary and conclusions are given in section 6.

2. Model description

a. Model

For this study we use version 5.0 of the Consortium for Small-Scale Modeling Model (COSMO-Model; Baldauf et al. 2011). The COSMO-Model is a nonhydrostatic, fully compressible limited-area atmospheric prediction model, designed for both operational high-resolution numerical weather prediction (NWP) and research applications on a broad range of spatial scales, from the mesoγ (horizontal scales between 2 and 20 km) to the mesoβ (horizontal scales between 20 and 200 km). The model is used in different configurations for operational numerical weather prediction purposes at several European weather services and has been further developed into a regional climate modeling system (Rockel et al. 2008).

We conduct simulations at horizontal grid spacings of 200 m (here referred to as COSMO-LES) and 1 km (COSMO-1). The time integration is performed with a third-order Runge–Kutta scheme (Klemp and Wilhelmson 1978; Wicker and Skamarock 2002). A fifth-order advection scheme is used for temperature, pressure, and horizontal and vertical winds, and a second-order scheme (Bott 1989) is employed for horizontal advection of moist quantities. The parameterizations include a radiative transfer scheme based on the δ-two-stream approach (Ritter and Geleyn 1992), in which radiation interacts with both subgrid- and grid-scale clouds, and a single-moment bulk microphysics scheme with three ice categories (ice, snow, and graupel) after Reinhardt and Seifert (2006).

Subgrid-scale turbulent mixing in COSMO-LES is parameterized by a 3D Smagorinsky–Lilly closure (Langhans et al. 2012c). COSMO-1 employs a 1D (vertical) turbulent scheme after Raschendorfer (2001). It is a 1.5-order scheme based on a prognostic equation for TKE with a level 2.5 closure, following Mellor and Yamada (1974, 1982). The different turbulence schemes tested in COSMO-1 during sensitivity studies are as follows: the 3D Smagorinsky–Lilly turbulence closure, a hybrid 1D–2D scheme that uses a Smagorinsky–Lilly closure in the horizontal and the 1D scheme in the vertical, and another 3D turbulence closure designed for LES (Deardorff 1973; Herzog et al. 2002). The latter utilizes a prognostic equation for subfilter-scale TKE. The tested convection parameterization is the Tiedke mass-flux scheme with moisture-convergence closure (Tiedtke 1989). The scheme distinguishes between shallow (restricted to a maximum depth of 250 hPa from the cloud base to the cloud top), midlevel, and deep convection. In our sensitivity studies for COSMO-1, only the shallow convection part of the scheme is turned on.

The atmospheric part of the system is coupled to the second-generation, 10-layer land surface model TERRA_ML (Heise et al. 2003), which provides values of surface temperature and specific humidity. A Louis surface transfer scheme (Louis 1979) is used to calculate the transfer coefficients that yield the surface sensible

TABLE 1. List of experiments and different configurations.

Expt	Δx	Orography	Configuration
LESf	200 m	None	3Dsmag
LESs5	200 m	Single 500 m	3Dsmag
LESd5	200 m	Double 500 m	3Dsmag
LESd15	200 m	Double 1500 m	3Dsmag
CRMd5	1 km	Double 500 m	1D, 1Dsh, hyb, 3Dsmag, 3Ddear
CRMd15	1 km	Double 1500 m	1D, 1Dsh, hyb, 3Dsmag, 3Ddear

TABLE 2. List of different CRM configurations.

Configuration	Turbulence scheme	Shallow convection scheme
1D	1D vertical + horizontal diffusion	Off
1Dsh	1D vertical + horizontal diffusion	On
hyb	1D vertical + 2D Smagorinsky horizontal	Off
3Dsmag	3D Smagorinsky	Off
3Ddear	3D Deardorff	Off

and latent heat fluxes based on the Monin–Obukhov similarity theory.

b. Setup

The model domain covers 380 km × 60 km. The horizontal grid spacing is 200 m in COSMO-LES and 1 km in COSMO-1, resulting in 1900 × 300 and 380 × 60 grid points in the horizontal, respectively. A generalized smooth level vertical (SLEVE) coordinate is used (Schär et al. 2002; Leuenberger et al. 2010). The vertical domain extends up to 21.5 km. COSMO-LES uses 177 vertical levels, and the grid spacing increases from 10 m at the lowest level to a maximum of 400 m at 21.5 km. COSMO-1 has 81 vertical levels, with vertical grid length varying from 20 m near the surface to 800 m above 18 km. The soil layer thickness varies from 2 cm to 5.76 m, and the soil total depth is 11.50 m. Soil parameters and plant characteristics are prescribed using equilibrated values from simulations of diurnal convection in a mid-European climate (Schlemmer et al. 2011). The time step is 2 s in COSMO-LES and 10 s in COSMO-1. The 3D fields are written every 6 min. The lateral boundary conditions are periodic in both horizontal directions. At the upper domain boundary a rigid lid is employed, and a Rayleigh damping layer extends from 11.5 km to the top of the domain to minimize spurious reflections of gravity waves. The Coriolis force is set to zero. To break the symmetry of the initial fields, the potential temperature is disturbed at the lowest model level with random perturbations of ±0.02 K. Incoming solar radiation is uniformly distributed on the entire domain and is determined for 48.25°N, 0° (which is comparable to the Black Forest region in central Europe) on 12 July 2006 following Schlemmer et al. (2011).

The case is based upon the setup introduced by Kirshbaum (2011), who constructed it from data retrieved during an intensive observational period (IOP 8b) from the Convective and Orographically Induced Precipitation Study (COPS) (Wulfmeyer et al. 2011). The initial temperature and moisture profiles are idealized from a COPS sounding that was launched at 0800 UTC [1000 local time (LT)] upstream of the southern Black Forest using a four-layer temperature profile and a three-layer humidity profile [see Fig. 1 in Kirshbaum (2011)]. The resulting initial flow is characterized by a stable layer up to 1 km, an elevated mixed layer (ML) between 1 and 3 km, a pseudoadiabatic layer up to 12.5 km, and a stable stratosphere. This makes the environment convectively inhibited (CIN ≈ 310 J kg^{-1}) and conditionally unstable, which are commonly observed features in Europe during summertime. The simulations start at 0600 LT and end at 2000 LT to capture the full diurnal cycle. To test the sensitivity to the background wind, we use a hyperbolic tangent profile for horizontal wind near the surface defined by

$$u(z) = u_{\max} \tanh(z/H), \tag{1}$$

where u is the horizontal wind speed, $u_{\max}$ = 1.5 or 3 m s^{-1}, z is the altitude (m), and H = 2000 m is a length scale. Two-dimensional topography, corresponding to two infinite ridges and an infinite valley in the y direction, is used. This provides more robust statistics by averaging in the y direction when necessary. The mountain profile used in this study is described in Schmidli et al. (2011). Two different valley depths of 500 m and 1.5 km, respectively, are employed, and the sloping sidewall width is set to 45 km. This leads to a crest-to-crest distance of 90 km. These numbers are chosen such that the idealized ridges roughly represent the dimensions of the Vosges–Black Forest mountain system. Furthermore, using a smooth terrain in both the CRM and LES minimizes the differences in their topographic representations. To allow for free development of the mountain–plain circulation without any interference from the model boundaries, the model domain is centered on the valley floor, and thus the flat terrain surrounding the mountain sector extends for 100 km away from the foothills.

The simulations and the different configurations are listed in Table 1 and Table 2. For the sensitivity studies

in section 5a, we have repeated each simulation three times for the CRM simulations and twice for the LES, using different initial random temperature perturbations at the lowest model level to check for robustness of the results with respect to turbulent fluctuations. Differences between the simulations were generally small, although there were some cases where the convection was slightly stronger over the western or eastern mountain in individual LESs. We use the mean of these simulations [denoted by asterisks (*)] in the discussion of several figures.

3. Methodology

a. The water vapor budget

The processes contributing to the instantaneous local moistening and drying of the BL atmosphere are given by

$$\frac{\partial q_v}{\partial t} = -\mathbf{v}\cdot\nabla q_v - \frac{1}{\rho l_v}(\nabla\cdot\mathbf{L}) + S_m, \tag{2}$$

where q_v is the specific water vapor, $\mathbf{v}$ is the wind speed vector, ρ is the air density, l_v is the latent heat of vaporization, $\mathbf{L} = \rho l_v \overline{\mathbf{v}'' q_v''}$ is the subgrid-scale latent heat flux, and S_m is microphysical source–sink rates (primarily condensation and evaporation of rain). The double prime indicates a subgrid-scale variable. All the terms in Eq. (2) are extracted using the moisture budget tool implemented in the COSMO-Model (Langhans et al. 2012a).

To compute the net effect of each process on a small control volume V of total mass M in the subcloud layer at the mountain top, Eq. (2) is integrated over V. The volume-averaged density-weighted water vapor budget equation is

$$\underbrace{\frac{1}{M}\int_V \rho\frac{\partial q_v}{\partial t}\,dV}_{\text{TOT}} = \underbrace{-\frac{1}{M}\int_V \rho\mathbf{v}\cdot\nabla q_v\,dV}_{\text{ADV}} + \underbrace{\frac{1}{M}\int_V -\frac{1}{l_v}(\nabla\cdot\mathbf{L})\,dV}_{\text{UNRES}} + \underbrace{\frac{1}{M}\int_V S_m\,dV}_{\text{MIC}}, \tag{3}$$

where TOT is the water vapor storage tendency, ADV is the water vapor advection, UNRES is the subgrid-scale latent heat flux convergence, and MIC is the microphysics contribution.

The total ADV can be further split into a horizontal (HADV) and vertical (ZADV) component:

$$\underbrace{-\frac{1}{M}\int_V \rho\mathbf{v}\cdot\nabla q_v\,dV}_{\text{ADV}} = \underbrace{-\frac{1}{M}\int_V \rho v_{\text{hn}}\cdot\nabla q_v\,dV}_{\text{HADV}} \underbrace{-\frac{1}{M}\int_V \rho w\cdot\nabla q_v\,dV}_{\text{ZADV}}, \tag{4}$$

where v_{hn} is the horizontal velocity component normal to the sidewalls (positive for inward-directed flow, negative for outward-directed flow), and w is the vertical velocity. In sections 4a and 4b the control volume is located over the western ridge summit (arbitrarily chosen over the eastern one, given the symmetry of the model domain), is 10 km wide in the x direction, and extends vertically from the surface up to the cloud base. Since the analysis in sections 4a and 4b is limited to the time period that precedes the onset of precipitation, the contribution of microphysical processes is neglected. In section 4d the control volumes are located over the foothills east and west of the mountain sector, are 30 km wide in the x direction, and extend vertically from the surface up to the BL top.

b. The subgrid-scale vertical fluxes of zonal momentum

In the CRM simulations, the subgrid-scale fluxes are computed by a 1D (vertical) turbulence scheme (see section 2a). If one defines τ_{uw} to be the subgrid-scale vertical component of the zonal turbulent momentum flux tensor (a similar parameterization applies to the meridional turbulent momentum flux tensor τ_{vw}) in the boundary layer approximation, it is parameterized as

$$\tau_{\text{uw}} = -\rho K_m^V \frac{\partial u}{\partial z}, \tag{5}$$

where K_m^V is the vertical diffusion coefficient or eddy viscosity, ρ is the air density, and u is the horizontal wind speed. The quantity K_m^V is determined using the Prandtl–Kolmogorov specification as

$$K_m^V = \phi_m \Lambda\sqrt{2\overline{e}}. \tag{6}$$

The characteristic length scale l for vertical mixing is calculated according to (Blackadar 1962):

$$l = \frac{kz}{1 + (kz)/l_\infty}, \tag{7}$$

where k is the von Kármán constant, and $l_\infty = 500$ m is an asymptotic length scale; ϕ_m is a stability-dependent coefficient, and $\overline{e} = (\overline{u_i'' u_i''})/2$, with $i = 1, 2, 3$, is the subgrid turbulent kinetic energy (TKE) per unit mass. The overbar denotes a time mean.

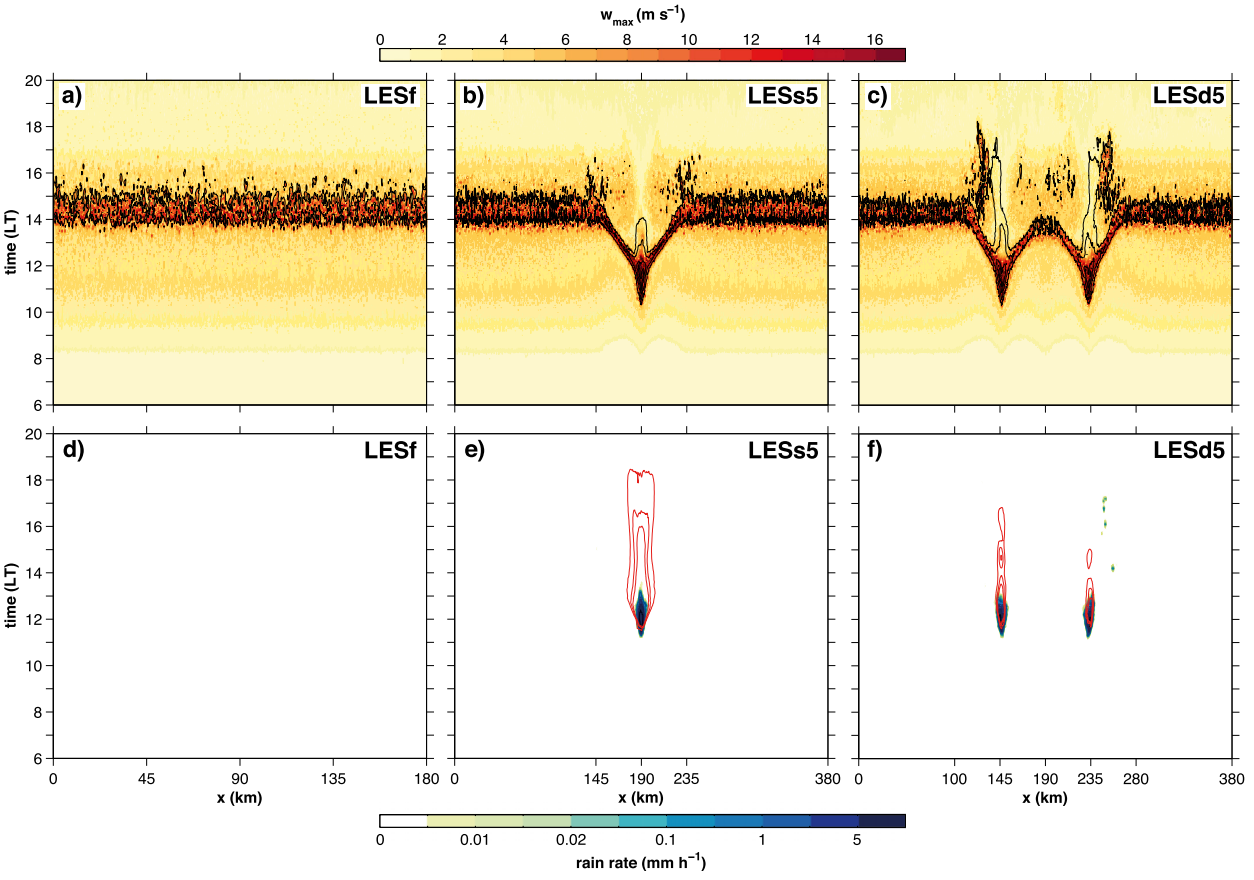

FIG. 1. (top) Hovmöller diagrams of maximum vertical velocity in the y–z plane (w_{max}; color scale) and y-averaged cloud liquid water path (black contours: 0.01, 0.1, 0.5, 1, 2, and 3 g kg^{-1}) for (a) LESf, (b) LESs5, and (c) LESd5. (bottom) Hovmöller diagrams of y-averaged surface rain rate (color scale) and cloud ice water path (red contours: 0.01, 0.02, and 0.03 g kg^{-1}) for (d) LESf, (e) LESs5, and (f) LESd5. In LESs5 and LESd5, the x-axis tick labels highlight the domain boundaries and the mountain sector: the mountain summits are located at $x = 190$ km in LESs5 and at $x = 145$ and $x = 235$ km in LESd5.

When run in LES mode, COSMO treats vertical and horizontal eddy viscosities with a 3D Smagorinsky–Lilly mixing-length turbulence model. For momentum fluxes, the residual stress tensor is defined as

$$\tau_{ij} = -2K_m D_{ij} \quad \text{and} \tag{8}$$

$$D_{ij} = \frac{1}{2}\left(\frac{\partial U_i}{\partial x_j} + \frac{\partial U_j}{\partial x_i}\right), \tag{9}$$

where D_{ij} is the grid-scale rate of strain. Here, isotropy is assumed. The eddy viscosity includes the effect of buoyancy and is given by

$$K_m = (c_s l_s)^2 \overline{D} \sqrt{\max\left(0, 1 - \frac{\mathrm{Ri}}{\mathrm{Ri}_c}\right)} \tag{10}$$

with the characteristic filtered rate of strain $\overline{D} = (2D_{ij}D_{ij})^{1/2}$ and the Smagorinsky length scale l_s given by Deardoff's proposal as $l_s = (\delta x \delta y \delta z)^{1/3}$. The Smagorinsky constant c_s in this study is set to 0.25; Ri_c is the critical Richardson number and Ri the deformation Richardson number, which is a function of moist static stability (see Langhans et al. 2012b).

4. Large-eddy simulations

a. Flow evolution and structure

To document the spatial distribution and time evolution of clouds and surface precipitation under the presence or absence of mountains, three LESs are compared: one with flat terrain only (LESf), one with an isolated single ridge (LESs5), and one with an isolated double ridge (LESd5). We begin by examining the case in which the mountain summits are at 500-m altitude, and are thus within the surface stable layer (see section 2b), and in which the background wind is absent.

The top panels in Fig. 1 are Hovmöller diagrams illustrating the onset time and spatial distribution of

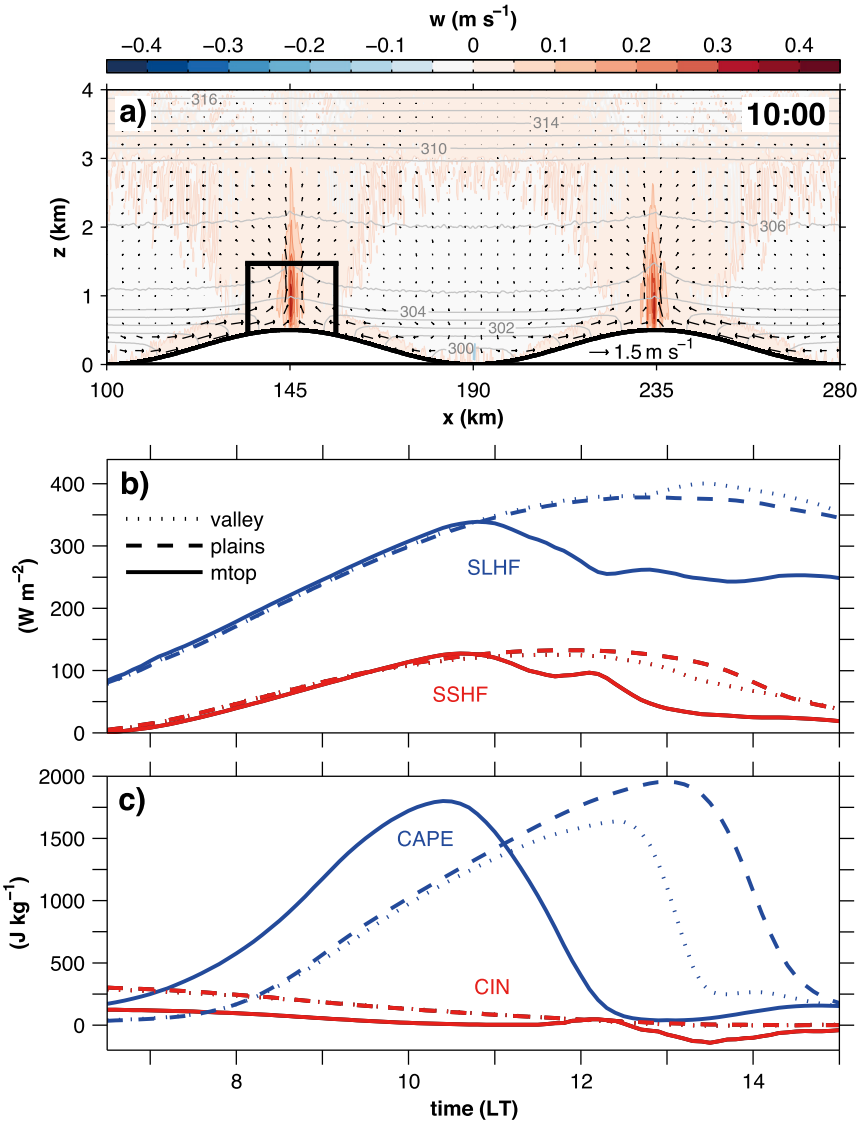

FIG. 2. (a) Hourly mean y-averaged wind speed (black vectors: reference vector of 1.5 m s^{-1}), potential temperature (K, gray lines) and vertical velocity (color scale) centered at 1000 LT in LESd5. The black box over the western mountain ridge displays the control volume used to compute the water vapor budget in Fig. 3a. (b),(c) Time evolution of y-averaged (b) SSHF (red lines) and SLHF (blue lines) and (c) CAPE (blue lines) and CIN (red lines) over the western mountain ridge (mtop; solid lines), over the valley center (dotted lines) and over the plains at $x = 50$ km (dashed lines).

updraft velocities and clouds. The bottom panels in Fig. 1 show the surface rain rate and the ice water path. The amount of cloud ice (at high levels) is an indicator of the presence of deep convective cells.

In LESf, the cloud liquid water path is very homogeneous, and a strong response of convection to the diurnal cycle of incoming solar radiation is observed: this starts with the development of a dry convective boundary layer, which is followed by shallow cumulus convection. The strongly inhibited environment (see section 2b) prevents the transition from shallow to deep convection, and no precipitation is produced throughout the whole simulation. In LESs5 shallow clouds are initiated in the morning at the mountain ridge summit by upslope wind convergence. Convective precipitation is generated just before noon. Over the surrounding plains, convection exhibits a diurnal cycle similar to the one in Fig. 1a for LESf except at the mountain ridge foot, where it is more intense and it lasts until the late afternoon. In LESd5 we observe similar features as in

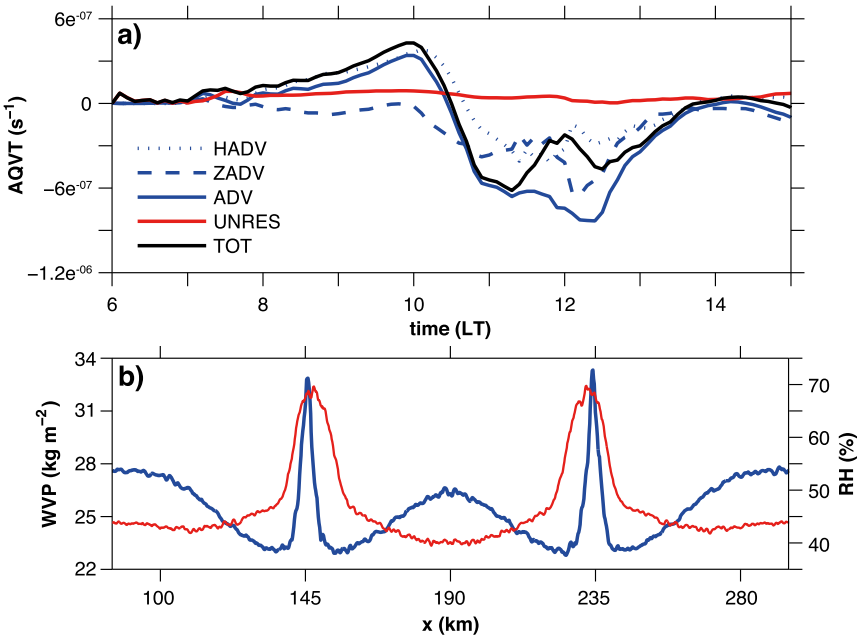

FIG. 3. (a) Time evolution of volume-averaged density-weighted water vapor tendencies in the control volume displayed in Fig. 2a. TOT (black line) is the storage tendency, HADV (dotted blue line) is the horizontal advection, ZADV (dashed blue line) is the vertical advection, ADV (solid blue line) is the total advection, and UNRES (red line) is the subgrid-scale latent heat flux convergence. (b) Horizontal distribution of y-averaged water vapor path (WVP; blue lines) and relative humidity at $z = 1500$ m (RH; red line) at 1100 LT in LESd5.

LESs5 at both mountain ridges, with convection and precipitation peaking at the summits. The deep convective events are less strong than the one in LESs5, as indicated by the smaller cloud ice content. Shallow clouds form over the valley in the afternoon, in response to relatively strong updraft motion.

Figure 2a illustrates the mean developing circulation over the mountain sector in LESd5. The circulation is driven by differential heating between the mountain summits and the surrounding air and is symmetric about the valley, owing to the lack of background wind. As in the simulations of Schmidli and Rotunno (2012) and Schmidli (2013), which did not include moist convection, the flow consists of weak mountain-to-plain and mountain-to-valley winds aloft and plain-to-mountain and valley-to-mountain winds below. Flow convergence and updrafts over the mountains and subsidence over the valley and over the foothills are also observed. Despite the presence of the mountains, the surface sensible (SSHF) and latent heat fluxes (SLHF) vary only slightly in the x direction (Fig. 2b); a significant reduction in both SSHF and SLHF is observed over the mountain summit only after the precipitation event. However, there is a considerable variation in both convective inhibition (CIN) and convective available potential energy (CAPE) in the x direction (Fig. 2c): CIN is lower, but CAPE is higher and builds up more efficiently over the mountain summit compared to over the surrounding terrain.

To quantify the respective contributions of the advective and unresolved terms in the water vapor budget equation [Eq. (3)] to the moistening of a control volume in the subcloud layer over the western mountain summit (see section 3a for a detailed description of the budget; the control volume considered is depicted in Fig. 2a), the time evolution of averaged specific water vapor tendencies within the control volume is shown in Fig. 3a. Until 1030 LT a net moistening of the control volume is observed. The major contribution comes from the horizontal advection, whereas a minor contribution is given by the unresolved fluxes, which mainly consist of surface latent heat flux and entrainment drying. Vertical advection is the only loss term: it represents vertical transport of moisture from the boundary layer into the midlevel troposphere, as well as resolved entrainment of dry air from the free troposphere into the subcloud layer. A sharp decrease in the horizontal advection contribution, which soon becomes a loss term, follows the onset of deep moist convection and precipitation.

Figure 3b shows the horizontal distribution of liquid water path (blue line; left axis) and relative humidity at $z = 1500$ m (red line; right axis) at 1100 LT in LESd5. At

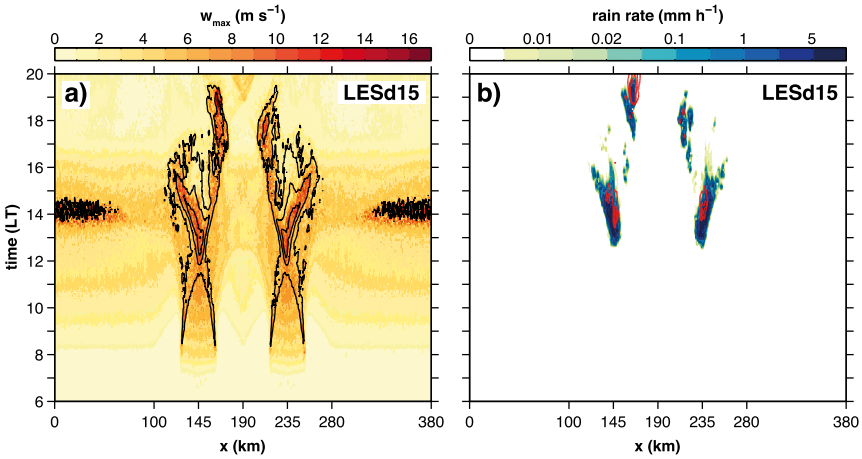

FIG. 4. (a),(b) As in Figs. 1c and 1f, but for LESd15.

the onset time of precipitation, the atmosphere above the mountain ridges has an excess of 5 kg m^{-2} of moisture compared to the surrounding plains and the valley, and relative humidity in the convective core exceeds that of the surrounding air by 25%.

b. *Mountain top embedded in an elevated mixed layer*

Figures 4a and 4b show the temporal and spatial distribution of updraft velocities, clouds, and precipitation in LESd15. By raising the mountain height to 1500 m, the summit breaks through the lower stable layer and is embedded within the elevated ML (see section 2b). By comparing the flow structure and evolution in Figs. 4a and 4b with those in Figs. 1c and 1f, important differences both before and after the first precipitation event over the mountain ridge summit are visible. First, updraft velocity peaks at the mountain slopes in the morning, and shallow clouds form there rather than at the summit. Second, in LESd15 convection moves toward the valley center in the afternoon, and two distinct secondary precipitation events can be seen over the valley sidewalls.

Figures 5a and 5b illustrate the evolution of the mean cross-ridge circulation over the mountain sector in LESd15 in the morning hours. In contrast to LESd5, the convective core at the summit is not isolated but rather located within a larger area of strong convection. In addition, vigorous convective cells are visible over the slopes. Within the elevated ML a neutrally stratified environment allows for vigorous BL turbulence. Convergence of mountain-to-valley winds at $z = 3$ km increases the subsidence between $z = 1$ and 3 km over the valley compared to over the plains. Both CIN and CAPE over the mountain summits are considerably lower compared to LESd5 (not shown), with the former being approximately zero throughout the whole simulation and the latter being roughly 100 J kg^{-1} (cf. Figure 2c) at the time of the first precipitation event.

Figure 5c shows the time evolution of averaged specific water vapor tendencies in a control volume in the subcloud layer at the western mountain summit in LESd15. The dimensions of the control volume considered are exactly as in LESd5 (see Fig. 2a and section 3a). In the morning, surface latent heating and vertical advection balance the negative contribution of horizontal advection (with the flow initially being downslope and toward the updrafts over the slopes; not shown). The observed peak in horizontal advection is delayed by roughly 2.5 h compared to LESd5. A large fraction of the moisture carried by upslope winds is removed vertically by the strong thermals over the mountain slopes once it enters the elevated ML and is therefore prevented from reaching the mountain top as in LESd5. This vertical transport of moisture leads to the formation of shallow cumuli over the mountain slopes, as illustrated in Fig. 4a, and can partially explain the delayed onset of deep convection compared to LESd5 observed in Figs. 4a and 4b. The reduced CAPE and the drier environment at the summit are also contributing factors. Note also that the peak in horizontal advection is much sharper compared to LESd5. This is explained by the convergence at the summit of the two convective cores over the slopes (see Fig. 5b).

c. *Deep precipitating convection over the valley sidewalls*

Differential heating processes between the valley atmosphere and the adjacent plains result in stronger upslope winds blowing from the plains compared to those blowing from the valley (Figs. 5a,b). The larger heating rate of the valley atmosphere can be explained from a bulk perspective in terms of the so-called

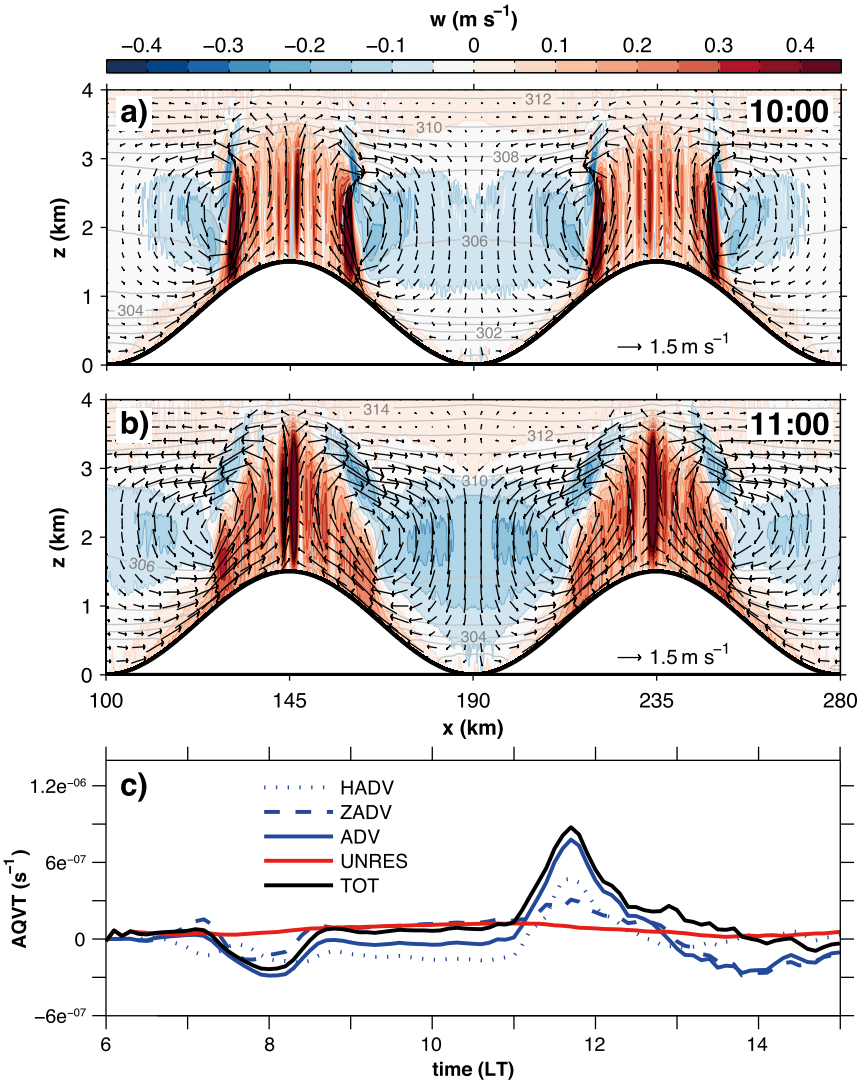

FIG. 5. (a),(b) Hourly mean *y*-averaged wind speed (black vectors: reference vector of 1.5 m s^{-1}), potential temperature (K, gray lines), and vertical velocity (color scale) centered at (a) 1000 and (b) 1100 LT in LESd15. (c) As in Fig. 3a, but for LESd15.

valley-volume effect (e.g., Wagner 1932): a certain amount of energy input applied to a valley heats a smaller volume and therefore a smaller mass of air compared to over flat terrain. Stronger subsidence over the valley compared to over the plains (see Figs. 5a,b) also contributes to explain the larger heating rate of the valley atmosphere. Figure 6a compares the time evolution of air temperature at a height of 1600 m in LESd15 at three different locations: over the valley center, over the eastern mountain summit, and over the open plains. The air over the mountain summit warms up faster than the surrounding air, triggering upslope winds at both mountain ridge slopes. However, the valley atmosphere heats up at a faster rate than the air above the plains, leading to a smaller temperature gradient and thus weaker upslope winds blowing from the plains compared to those blowing from the valley. This difference is important in determining the flow evolution after the first precipitation event over the mountain summit.

Cooling by evaporation of precipitation below convective clouds results in cold pools, which are characterized by a near-surface horizontal flow of relatively cold and dry air. A few studies (e.g., Grabowski et al. 2006; Khairoutdinov and Randall 2006; Böing et al. 2012; Bao and Zhang 2013; Schlemmer and Hohenegger 2014) investigated how precipitation-driven cold pools aid the transition from shallow to deep convection. Vertical lifting and moisture accumulation at the leading edge of the cold pool play an important role. Kirshbaum

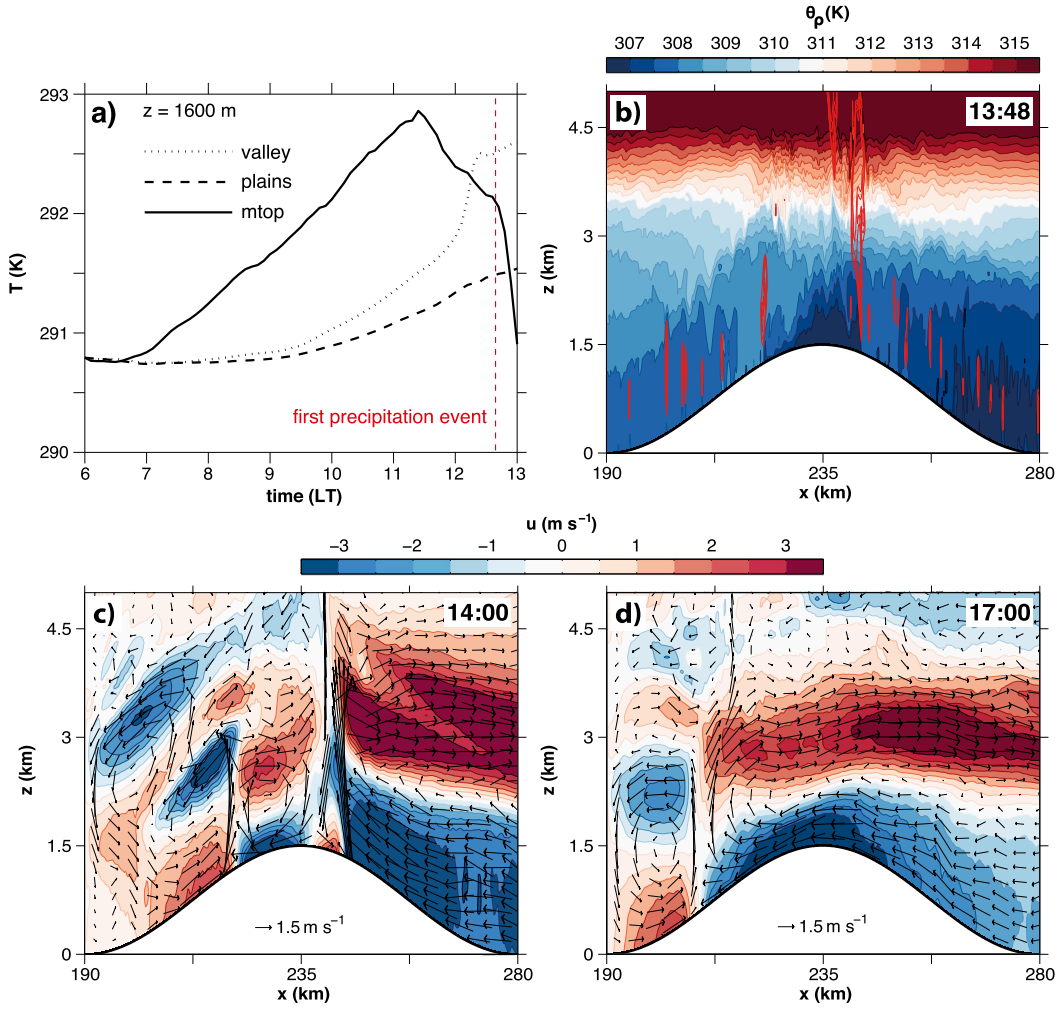

FIG. 6. (a) Time evolution of y-averaged air temperature at 1600-m altitude above the valley (dotted line), above the eastern mountain ridge (solid line), and above the plains at $x = 280$ km (dashed line) in LESd15. The vertical red line indicates the time of the first precipitation event over the eastern mountain ridge summit. (b) Vertical cross section at $y = 0$ km of density potential temperature (θ_ρ; color scale) and updraft velocity (red contours: 2, 2.5, 3, and 3.5 m s^{-1}) after the first precipitation event over the eastern mountain ridge summit. (c),(d) Vertical cross sections of y-averaged horizontal velocity (color scale) and wind speed (black vectors: reference vector of 1.5 m s^{-1}) (c) after the first precipitation event and (d) before the second precipitation event over the eastern mountain ridge in LESd15.

and Grant (2012) remarked the importance of this feedback in studies of orographic convection.

Figure 6b displays density potential temperature θ_ρ and updraft velocity after the first precipitation event over the eastern ridge in LESd15; θ_ρ is defined as

$$\theta_\rho \equiv T_\rho \left(\frac{p_0}{p}\right)^{R_d/c_{\mathrm{pd}}}, \tag{11}$$

where T_ρ is the density temperature, p_0 is a standard reference pressure of 1000 hPa, p is the pressure, R_d is the gas constant for dry air, and c_{pd} is the heat capacity of dry air at constant pressure. Following Emanuel (1994), the density temperature is defined as

$$T_\rho \equiv T \frac{1 + r/\varepsilon}{1 + r_T}, \tag{12}$$

where r is the water vapor mixing ratio, $\varepsilon = R_d/R_v$ is the ratio between the gas constant for dry air and for water vapor, and $r_T = r + r_l + r_i$ is the net water mixing ratio, which includes ice and liquid water. The value of T_ρ may thus be either greater than or less than the actual temperature T depending on the relative amounts of condensed water and water vapor. The cold pools are visible as the region of low θ_ρ at the mountain summit in Fig. 6b. Forced lifting along the leading edges of the downslope-traveling cold pools is highlighted by the red contours at $x = 220$ and 245 km.

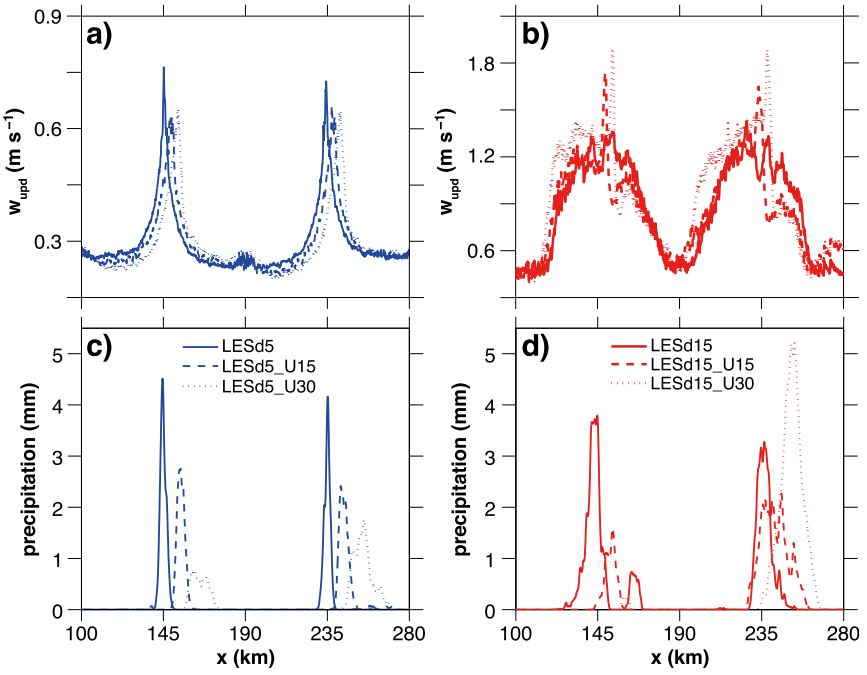

FIG. 7. (a),(b) Hourly mean updraft velocities w_{upd} averaged in the y direction and over the first kilometer above the mountain summits centered (a) at 1100 LT in LESd5 (solid line) and (b) at 1500 LT in LESd15 (solid line) with increasing background wind: _U15 (dashed line) and _U30 (dotted line). (c),(d) As in (a),(b), but for the y-averaged accumulated surface precipitation over the entire duration of the simulation.

Figures 6c and 6d illustrate the flow evolution over the eastern mountain ridge between the first precipitation event over the summit and the second precipitation event over the valley sidewall. Stronger low-level convergence is observed after the first precipitation event over the mountain slope toward the plains compared to over the valley sidewall (cf. the upward motion at $x = 220$ and at $x = 245$ km in Figs. 6b,c). However, the flow field becomes rapidly dominated by upslope winds again toward the plains, whereas over the valley sidewall the weaker upslope winds allow the cold pool to travel downslope (see Fig. 6d). Stronger updrafts are driven by wind convergence at the leading edge of the cold pool when it collides with the upslope flow and generate the secondary precipitation event.

d. *The role of background wind in convection initiation*

The background wind speed U_b not only controls the strength of the mass convergence over the mountain top (e.g., Crook and Tucker 2005; Kirshbaum 2011), but also the moisture distribution within the mountain sector. Given the importance of this parameter, its influence on the simulated cloud and precipitation fields is investigated. The strength of the background wind (see section 2b) is gradually increased in LESd5 and LESd15.

Figures 7a and 7c illustrate the strength and location of the thermally induced updrafts over the mountain summits in the morning and the spatial distribution of accumulated precipitation over the mountain sector in LESd5 with increasing background winds. The updrafts are strongest and develop at the summit without background wind. As the background wind increases, the updrafts weaken and form farther down the downwind slope. The weaker convective cores generate less intense rainfall in LESd5_U15 and LESd5_U30. In contrast in LESd15, in which the mountains are higher and generate stronger circulations compared to LESd5, the updrafts over the mountain summits strengthen with increasing background wind (Fig. 7b), and the spatial distribution of precipitation over the downwind mountain ridge exhibits a different pattern than the one observed in Fig. 7c and over the upwind mountain ridge (Fig. 7d). As U_b increases, precipitation in LESd15 decreases upwind but increases downwind of the valley.

Figure 8a illustrates the specific water vapor and wind velocity fields at 1200 LT in LESd15_U30. The background wind has been removed here to better illustrate the circulations associated with the convective cores over the mountain slopes. The convective

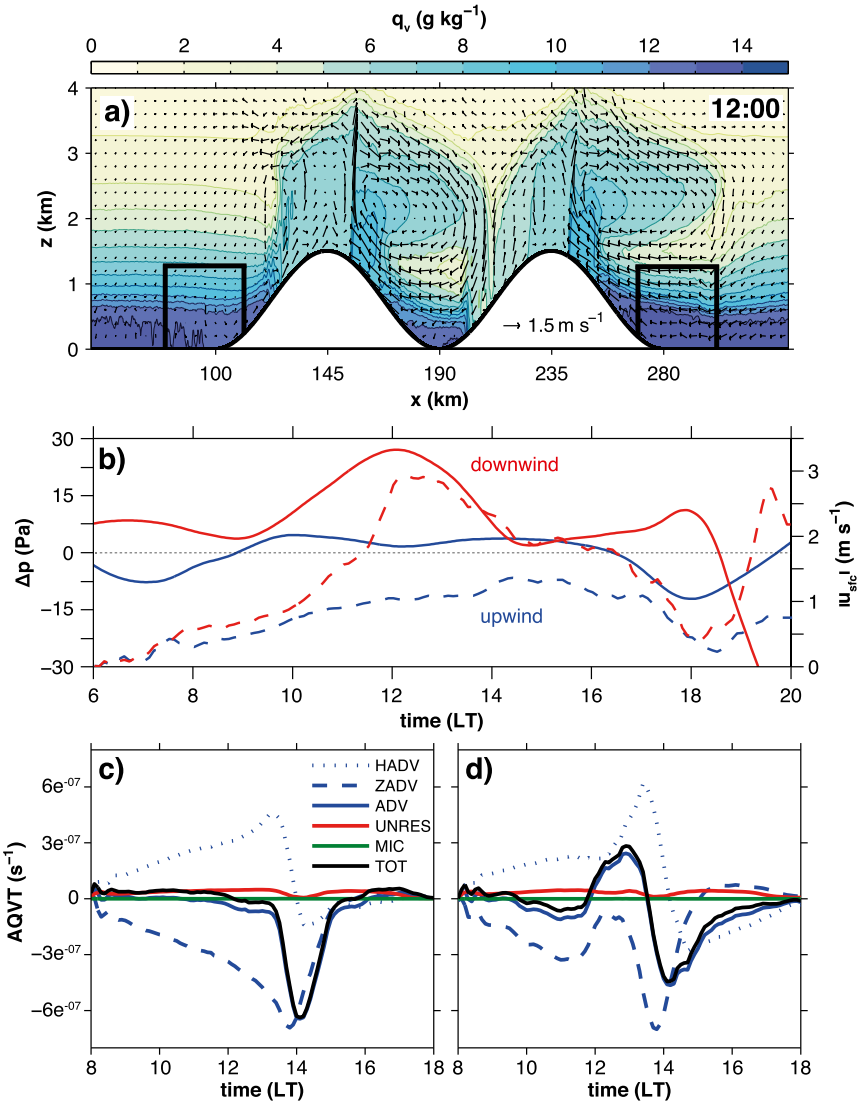

FIG. 8. (a) Vertical cross section at $y = 0$ km of specific water vapor q_v (color scale) and cross-ridge wind speed (black vectors: reference vector of 1.5 m s^{-1}) at 1200 LT in LESd15_U30. The black boxes over the foothills downwind and upwind of the mountain sector display the control volumes used to compute the water vapor budget in Figs. 8c and 8d. (b) Time evolution of y-averaged pressure gradient between the plains (40 km away from the foothills) and the foothills (solid lines; left vertical axis) and absolute horizontal wind speed at a height of 20 m $|u|_{sfc}$ (dashed lines; right vertical axis) upwind (blue lines) and downwind (red lines) of the mountain sector. (c),(d) Time evolution of y-averaged water vapor tendencies in the (c) upwind and (d) downwind control volume depicted in Fig. 8a.

circulations perturb the basic pressure state and ultimately drive changes in the low-level flow. Figure 8b compares the surface pressure gradient between the plains and the foothills (solid lines; left axis) and the low-level horizontal wind speed (dashed lines; right axis) upwind and downwind of the mountain sector. The convective core at $x = 240$ km is located over the mountain slope on the lee side of the mountain sector; the associated upward motion generates a low surface pressure perturbation over the foothills, and a high surface pressure perturbation over the open plains, as a result of compensating subsidence. This strengthens the surface pressure gradient on the lee side of the mountain sector, which ultimately leads to a stronger low-level flow toward the mountains. Note that a stronger low-level flow is also observed upwind of the valley compared to downwind of the valley and is generated by the same mechanism discussed above.

This explains the strengthening of the updrafts at both mountain summits observed in Fig. 7b.

An asymmetric spatial distribution similar to the one illustrated in Fig. 7d for the accumulated precipitation in LESd15 is observed in Fig. 8a in the water vapor field and can be explained by the combined effects of the compensating subsidence associated with the convective circulation and the strengthening of the low-level flow toward the mountains on the lee side. Figures 8c and 8d compare the moisture tendencies in two control volumes within the boundary layer over the foothills (see the black boxes in Fig. 8a), one upwind (Fig. 8c) and one downwind (Fig. 8d) of the mountain sector. Before the onset of precipitation, a balance between a net positive contribution of horizontal advection and the negative contribution of vertical advection is observed in both control volumes. However, after 1130 LT, a decrease in export due to vertical advection and an increase in import due to horizontal advection are observed in the control volume downwind of the mountains. This is the combined effect of the compensating subsidence from the circulation associated with the convective core over the mountain slopes and the strengthening of low-level flow toward the mountain foothills, which not only carries BL moisture from the open plains, but also disturbs the development of diurnal BL convection over the foothills. This extra availability of water vapor on the lee side explains the observed spatial distribution of convection and precipitation. Note that when the accumulated water vapor is transported over the mountain summit, CAPE also increases from the low values observed in LESd15 up to roughly 600 J kg^{-1} (not shown).

5. Convection-resolving simulations

The simulations discussed in sections 4a, 4b, and 4c are repeated with a CRM setup using a horizontal grid spacing of 1 km to investigate the performance of a coarser-resolution model in reproducing the spatial and temporal evolution of convection and precipitation. Figures 9a–d illustrate the evolution of convection and precipitation in CRMd5 (Figs. 9a,c) and CRMd15 (Figs. 9b,d). The most important physical processes described in sections 4a, 4b, and 4c are captured: the first precipitation events at the mountain top, the downslope-traveling cold pools, and the secondary precipitation events over the valley sidewalls in LESd15. Nevertheless, the absence of shallow cumuli in the morning over the slopes and an earlier triggering of convective precipitation are observed in CRMd15. In particular, the first precipitation event at the mountain top occurs 1 h earlier, and the secondary precipitation event over the valley sidewalls three hours earlier.

Figures 9e and 9f show the time evolution of averaged specific water vapor tendencies in CRMd5 and CRMd15 in the same control volume in the subcloud layer over the western mountain summit used in the analysis in sections 4a and 4b. Although there are only minor differences comparing CRMd5 with LESd5, in CRMd15 an earlier, sharper, and stronger (roughly twice as large) horizontal water vapor advection toward the mountain summit compared to LESd15 is observed (cf. Fig. 3a for LESd5 and Fig. 5c for LESd15).

Figures 10a and 10b compare vertical velocity, potential temperature, and the mean cross-ridge wind speed over the western slope of the western mountain ridge at 1030 LT in (Fig. 10a) LESd15 and (Fig. 10b) CRMd15. Instantaneous values of vertical velocity are shown to illustrate the BL thermals. In CRMd15, a distinct updraft is observed at the mountain summit. In LESd15, the BL thermals are explicitly resolved, and a transition between less intense convection over the mountain slopes and more vigorous convection over the mountain top, where the upslope winds converge, is observed. The enhanced vertical motion within the elevated ML seen in LESd15 is only partially observable in the coarser-resolution simulation. Also, resolved mixing at the BL top seen in LESd15 is absent in CRMd15.

Vertical turbulent transport by BL thermals removes some of the water vapor but also momentum from the upslope flow. The turbulent (resolved + unresolved: see section 3b for the computation of the unresolved fluxes) vertical fluxes of zonal momentum at $x = 135$ km (within the elevated ML) and at a height of 20 m in LESd15 and CRMd15 are compared in Fig. 10c. The resolved turbulent fluxes are calculated offline as deviations from the mean thermally driven circulation. The total (resolved + unresolved: solid lines) fluxes are larger in LESd15 than in CRMd15, which suggests a stronger vertical transport of momentum in the higher-resolution runs. Figure 10d compares the time evolution of the horizontal wind speed at the same location where the vertical turbulent fluxes of momentum are computed in the morning in LESd15 and CRMd15. Weaker vertical transport within the elevated ML in CRMd15 leads to stronger horizontal wind velocities compared to the LES. This not only strengthens mass convergence over the mountain summit, but also explains the stronger horizontal water vapor advection observed in Fig. 9f. Reduced lateral turbulent entrainment in rising thermals as a result of the coarser resolution (not shown) could have also contributed to more vigorous convection in CRMd15. Recently, Hohenegger et al. (2015) also found a faster transition in coarser-resolution simulations, but in contrast they observed a delayed

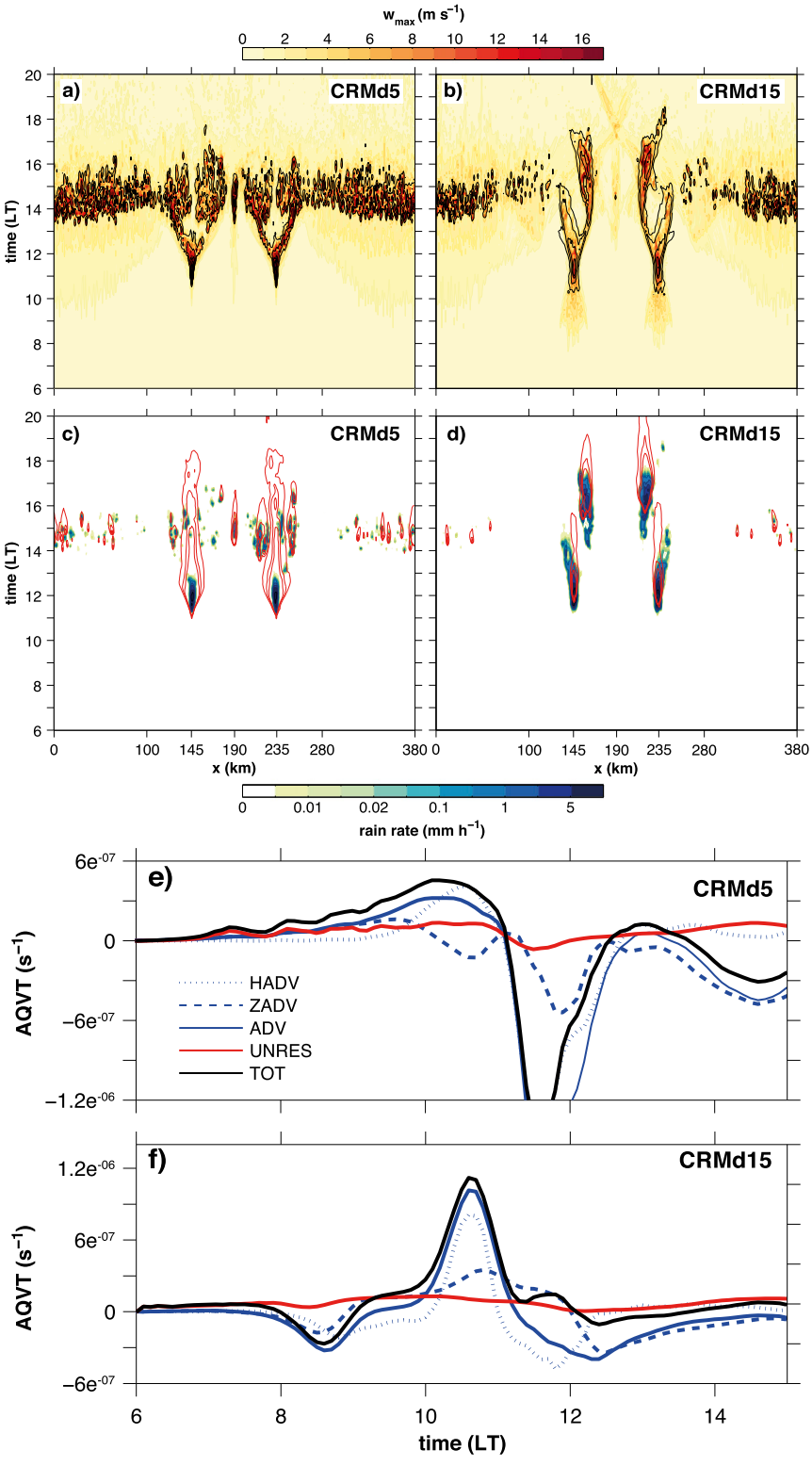

FIG. 9. (a)–(d) As in Figs. 1c and 1f, but for (a),(c) CRMd5 and (b),(d) CRMd15. (e),(f) As in Fig. 3a, but for (e) CRMd5 and (f) CRMd15.

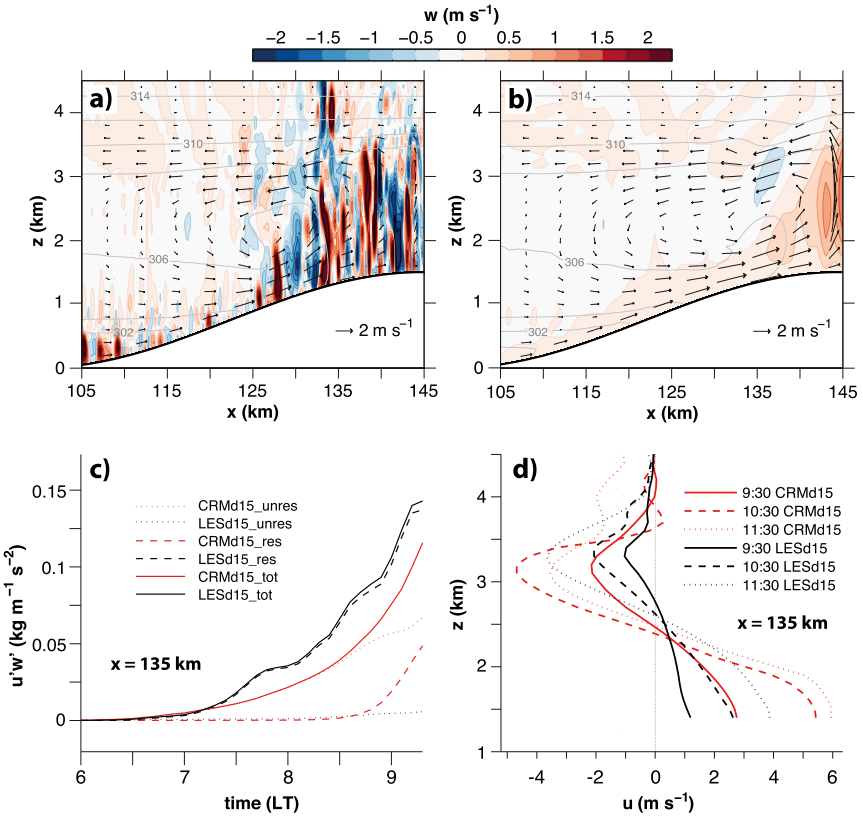

FIG. 10. (top) Vertical cross sections of instantaneous vertical velocity (color scale) at 1030 LT and hourly mean y-averaged wind speed (black vectors: reference vector of 2 m s^{-1}) and potential temperature (K, gray contours) centered at 1030 LT in (a) LESd15 and (b) CRMd15. (c) Time evolution of y-averaged vertical turbulent fluxes of momentum in LESd15 (black lines) and CRMd15 (red lines) at x = 135 km and at a height of 20 m. The legend discriminates between unresolved (dotted lines), resolved (dashed lines), and total (resolved + unresolved) fluxes. (d) Hourly mean vertical profiles of y-averaged horizontal wind speed centered at 0930 (solid lines), 1030 (dashed lines), and 1130 LT (dotted lines) in LESd15 (black lines) and CRMd15 (red lines) at x = 135 km.

development of convection for the sea-breeze system studied.

Sensitivity to the turbulence and shallow convection parameterization

The sensitivity of precipitation and horizontal wind velocity in the CRM simulations to different turbulence parameterizations and to the employment of a shallow convection scheme is investigated.

The top panels in Fig. 11 compare the time evolution of the domain-averaged surface rain rate in d5, d15, and d15_U3.0, which include both the LES and CRM experiments. The middle panels in Fig. 11 show the spatial distribution of the accumulated precipitation at the surface during the entire duration of the simulations. The differences are small between CRMd5 and LESd5, in which vertical motion is limited within the shallow boundary layer, but there are big differences between CRMd15 and LESd15, in which convection is enhanced within the elevated ML.

The spatial distribution of precipitation is strongly controlled by the orography and is almost independent of the choice of the turbulence parameterization scheme. In contrast, the onset timing of precipitation differs by up to several hours. Three-dimensional schemes systematically delay the onset of convective precipitation in the CRM simulations. The differences are generally small between 1D* and hyb*, but larger differences are found when comparing these two schemes with 3Dsmag* and 3Ddear*, and also between 3Dsmag* and 3Ddear* themselves, suggesting that the choice of the horizontal mixing formulation may not account for the main differences between 1D and 3D schemes. In LESd5 and CRMd5, where the mountain slopes are less steep and the circulations develop mainly in the horizontal, there is stronger resemblance between the LES and the CRM simulations

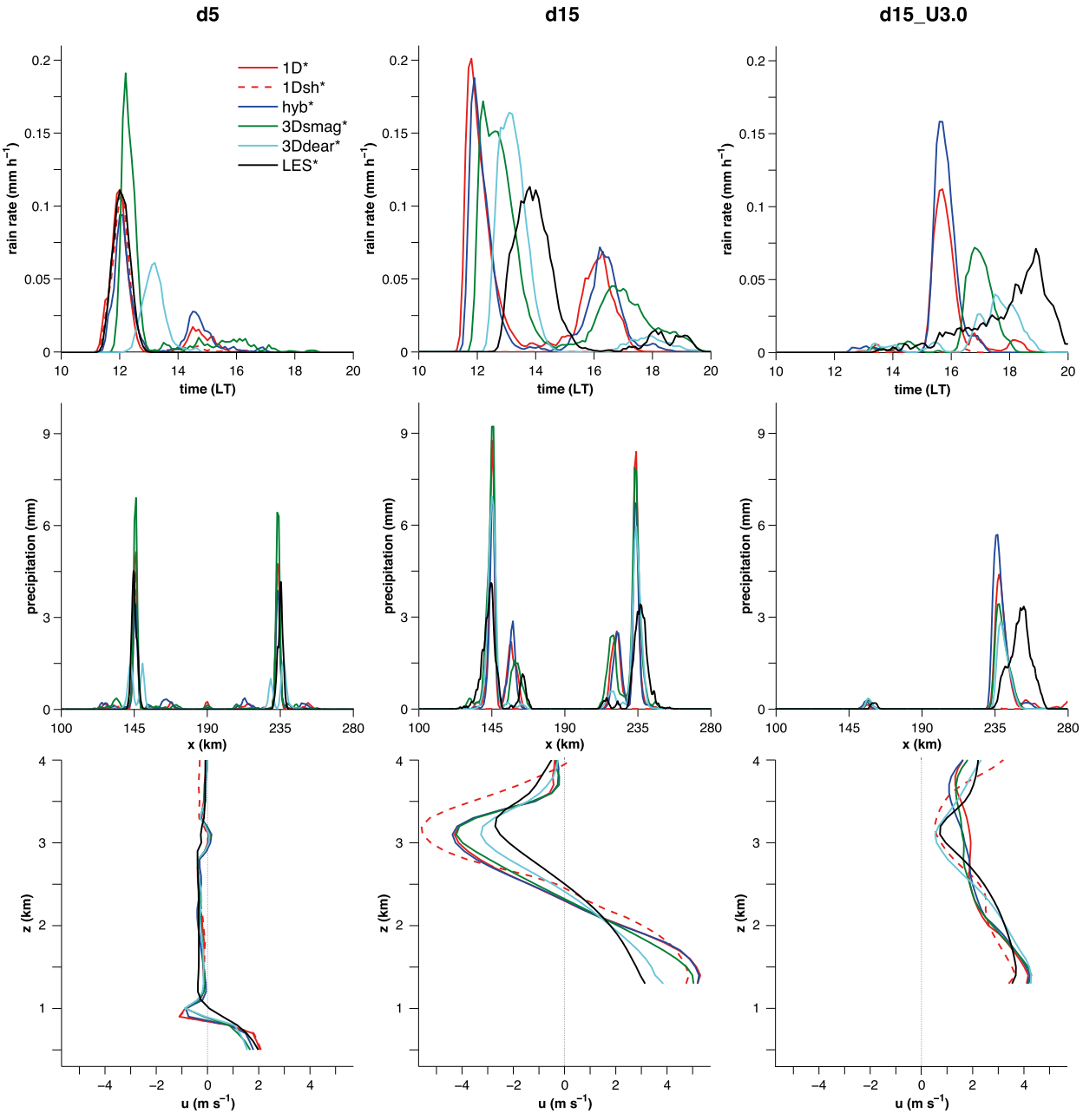

FIG. 11. (top) Time evolution of ensemble- and domain-averaged surface rain rate in (left to right) d5, d15, and d15_U3.0. (middle) As in (top), but for the ensemble- and y-averaged accumulated surface precipitation over the entire duration of the simulation. (bottom) As in (top), but for the running hourly mean vertical profiles of ensemble- and y-averaged horizontal wind speed at $x = 135$ km centered at 1030 LT.

employing a 1D turbulence scheme as compared to CRM simulations employing a 3D scheme. A 3D turbulence scheme seems more suitable in CRMd15 and in CRMd15_U3.0, in which the onset time of precipitation is strongly influenced by vertical transport processes by the BL eddies.

The bottom panels in Fig. 11 compare vertical profiles of horizontal wind speed over the mountain slopes at 1030 LT. The differences between the simulations are marginal in d5 and d15_U30. In d15, in the CRM simulations employing a 3D turbulence scheme the upslope winds are weaker compared to CRM simulations employing a 1D turbulence scheme, suggesting an increased vertical mixing. This could explain the delayed onset of precipitation observed in the panel above.

The employment of a shallow convection scheme (1Dsh*) does not modify substantially the simulated flow evolution in CRMd5 but has a big impact in

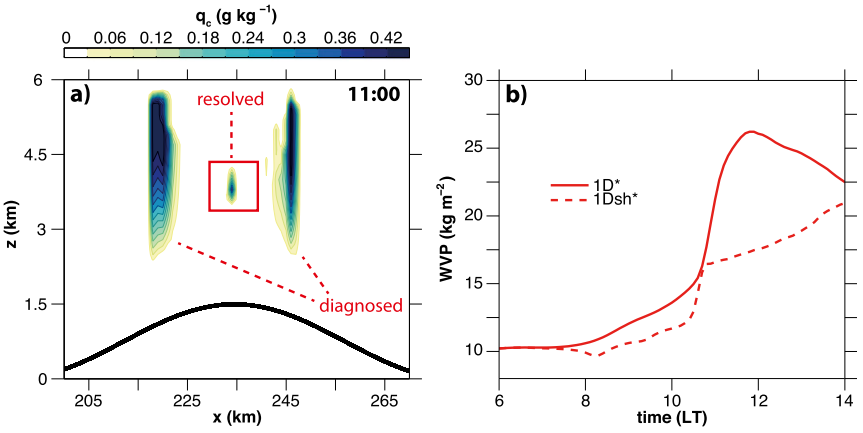

FIG. 12. (a) Vertical cross section of y-averaged specific cloud liquid water content q_c (color scale) at 1100 LT over the eastern mountain ridge in 1Dsh. The red labels point at the parts of the cloud field that are explicitly resolved and diagnosed by the shallow convection scheme. (b) Time evolution of the y-averaged water vapor path over the eastern mountain ridge summit in 1D* (solid line) and 1Dsh* (dashed line).

CRMd15 and CRMd15_U3.0, in which precipitation is almost absent. The thick clouds visible over the slopes and diagnosed by the scheme in Fig. 12a are absent in the LES (cf. Fig. 4a for LESd15). In Fig. 12b, which shows the time evolution of water vapor path above the mountain summit, a less pronounced moistening of the mountain summit is observed in the morning hours in 1Dsh* compared to 1D*. The scheme thus seems to exhibit a strong sensitivity to grid-scale moisture convergence in the subcloud layer. The authors observed a partial improvement, at least in the representation of the cloud field, changing the mass-flux closure to a surface buoyancy flux-based one (not shown).

6. Summary and conclusions

The important mechanisms of moist convection initiation and precipitation development within thermally driven wind systems over mountainous terrain are investigated in large-eddy (LES) and convection-resolving (CRM) simulations over an idealized double-ridge system with an embedded valley. For this study the model of the Consortium for Small-Scale Modeling (COSMO-Model) is run at horizontal grid spacings of 200 m and 1 km. The simulations are based on the setup introduced by Kirshbaum (2011). The strong convective inhibition, the presence of an elevated mixed layer (ML), and the conditional instability of the flow make it a useful case study to gain insight into orographic controls on cloud formation and the triggering of precipitation.

First, the mechanisms are analyzed by means of LES. Mass convergence, a more efficient buildup of CAPE, and a weaker inhibition over the mountains flanking the valley combine with water vapor advection by upslope winds to initiate deep convection. Over higher mountains, whose summits protrude above the early morning lower stable layer and into the elevated ML, the transition to deep, precipitating convection is delayed compared to simulations with lower mountains, although convection inhibition is reduced. The delayed precipitation is mainly associated with increased vertical mixing within the elevated ML, which delays water vapor advection toward the mountain summits by upslope winds. A drier environment and a reduced CAPE over the mountain summits also contribute to explain the delayed precipitation. In the afternoon, secondary precipitation events are observed over the valley slopes. Differential heating processes between the valley atmosphere and the adjacent plains result in stronger upslope winds blowing from the plains compared to those blowing from the valley. This results in a preferential propagation of precipitation-driven cold pools at the summits toward the valley center. A strengthening of low-level convergence over the valley sidewalls is observed when the downslope-traveling cold pools collide with the upslope winds, which triggers the observed deep, precipitating convection.

The presence of background wind moves the convective cores over the slopes downwind of the summits, weakens convective updraft strength, and reduces the amount of accumulated precipitation in the simulations with lower mountains. However, in the simulations with higher mountains the updraft strengthens with increasing background wind, and an asymmetric spatial distribution of precipitation is observed, with lower precipitation over the upwind ridge and higher precipitation over the downwind ridge and on the lee side of

the mountain sector for stronger ambient winds. The perturbation induced in the pressure field by the downwind shifting of the convective cores strengthens the updrafts downwind of the mountain summits, and in particular the low-level flow on the lee side, which transports moisture from the plains toward the mountains. This causes a massive moisture accumulation and a preferential location for the onset of deep moist convection over the downwind ridge and on the lee side of the mountain sector.

In the second part of the study, CRM simulations are run and compared to the LES to investigate the performance of a coarser-resolution model in reproducing the mechanisms described above. Both the total precipitation amount and its spatial distribution simulated in the LES are well captured in CRM simulations with low mountains, in which vertical motion in the morning is limited within the shallow surface ML, and the circulations develop mainly in the horizontal. When the mountains are sufficiently high to enter the elevated ML, a faster triggering of deep convection and an earlier onset of precipitation are observed in the CRMs. The CRMs have a too-coarse grid spacing to resolve the boundary layer eddies simulated in the LES, which remove some of the moisture and horizontal momentum from the upslope flow by vertical turbulent transport, and tend to underestimate the unresolved fluxes. This results in stronger upslope winds and stronger horizontal water vapor advection toward the mountain summit in the CRM simulations, which ultimately explain the faster and sharper transition from shallow to deep convection and the earlier development of precipitation compared to the LES.

Several CRM ensembles employing different turbulence parameterization schemes are also compared. The turbulence parameterization scheme is found to have a minor influence on the spatial distribution of precipitation. However, there are differences in the onset time of convective precipitation and in the simulated surface rain rate compared to the LES. In particular, the employment of a 3D turbulence parameterization scheme is observed to systematically lead to weaker upslope winds, suggesting increased vertical mixing and delaying the onset of convective precipitation. The sensitivity studies also suggest that the different behaviors between the turbulence schemes might be due to differences in the vertical mixing formulation, rather than in the horizontal. The employment of a shallow convection scheme delays and dramatically reduces the precipitation when the mountain summit is located within the elevated ML. This is due to an excessive vertical moisture transport over the mountain slopes compared to the LES and other CRM simulations in which the shallow convection scheme is not active.

To conclude, the case setup chosen allowed for analyzing particular interactions and feedbacks that led to important differences between the LES and the CRMs. The choice of a double mountain ridge was made to capture features of real orographic systems, such as differential heating processes between the valley and the surrounding plains. The full treatment of moist convection and of cloud-radiation feedbacks represented a step forward toward a more complete analysis with respect to previous similar studies. Also, the consideration of land–atmosphere interactions allowed for a more realistic representation of feedbacks between clouds and surface fluxes compared to other studies that used prescribed surface fluxes.

Further research is necessary to confirm the relative importance of the convection initiation and precipitation development mechanisms described in this study. In this study, the presence and depth of the elevated ML certainly had an impact on the simulated amounts of precipitation. The analysis in the presence of a background wind can be further improved by considering 3D topography with finite ridges to allow for other important effects, such as leeside convergence, that are not considered in this study. Small-scale topographical variations can also affect the orographic flow evolution because of channeling effects or strong local convergence at isolated small-scale peaks (e.g., Kirshbaum et al. 2007; Fuhrer and Schär 2007) and lead to further issues concerning turbulence parameterization (Rotach and Zardi 2007).

Acknowledgments. Funding for Davide Panosetti and Linda Schlemmer was provided by ETH *Zürich*. Funding for Steven Böing and Jürg Schmidli was provided by MeteoSwiss through C2SM (ETH *Zürich*). Steven Böing was further funded through a joint University of Leeds/Met Office fellowship. Jürg Schmidli was also partly supported by the Hans Ertel Centre for Weather Research. This research network of universities, research institutes and the German Weather Service (DWD) is funded by the Federal Ministry of Transport and Digital Infrastructure (BMVI).

The numerical simulations have been performed on the Cray XC30 (Piz Daint) at the Swiss National Supercomputing Centre (CSCS). Access to the COSMO-Model was kindly provided by the Consortium for Small-Scale Modeling. The authors acknowledge Prof. Dr. Christoph Schär and Prof. Dr. Tapio Schneider for the helpful discussions and comments on the manuscript. Constructive comments have been provided by three anonymous reviewers. The authors thank MeteoSwiss and Daniel Lüthi for their technical support.

REFERENCES

Baldauf, M., A. Seifert, J. Förstner, D. Majewski, M. Raschendorfer, and T. Reinhardt, 2011: Operational convective-scale numerical weather prediction with the COSMO model: Description and sensitivities. *Mon. Wea. Rev.*, **139**, 3887–3905, doi:10.1175/MWR-D-10-05013.1.

Ban, N., J. Schmidli, and C. Schär, 2014: Evaluation of the convection-resolving regional climate modeling approach in decade-long simulations. *J. Geophys. Res. Atmos.*, **119**, 7889–7907, doi:10.1002/2014JD021478.

Banta, R. M., 1984: Daytime boundary-layer evolution over mountainous terrain. Part I: Observations of the dry circulations. *Mon. Wea. Rev.*, **112**, 340–356, doi:10.1175/1520-0493(1984)112<0340:DBLEOM>2.0.CO;2.

——, 1990: The role of mountain flows in making clouds. *Atmospheric Processes over Complex Terrain*, Meteor. Monogr., No. 23, Amer. Meteor. Soc., 229–282.

Bao, X., and F. Zhang, 2013: Impacts of the mountain–plains solenoid and cold pool dynamics on the diurnal variation of warm-season precipitation over northern China. *Atmos. Chem. Phys.*, **13**, 6965–6982, doi:10.5194/acp-13-6965-2013.

Blackadar, A. K., 1962: The vertical distribution of wind and turbulent exchange in a neutral atmosphere. *J. Geophys. Res.*, **67**, 3095–3102, doi:10.1029/JZ067i008p03095.

Böing, S. J., H. J. Jonker, A. P. Siebesma, and W. W. Grabowski, 2012: Influence of the subcloud layer on the development of a deep convective ensemble. *J. Atmos. Sci.*, **69**, 2682–2698, doi:10.1175/JAS-D-11-0317.1.

Bott, A., 1989: A positive definite advection scheme obtained by nonlinear renormalization of the advective fluxes. *Mon. Wea. Rev.*, **117**, 1006–1016, doi:10.1175/1520-0493(1989)117<1006:APDASO>2.0.CO;2.

Brockhaus, P., D. Lüthi, and C. Schär, 2008: Aspects of the diurnal cycle in a regional climate model. *Meteor. Z.*, **17**, 433–443, doi:10.1127/0941-2948/2008/0316.

Bryan, G. H., J. C. Wyngaard, and J. M. Fritsch, 2003: Resolution requirements for the simulation of deep moist convection. *Mon. Wea. Rev.*, **131**, 2394–2416, doi:10.1175/1520-0493(2003)131<2394:RRFTSO>2.0.CO;2.

Craig, G. C., and A. Dörnbrack, 2008: Entrainment in cumulus clouds: What resolution is cloud-resolving? *J. Atmos. Sci.*, **65**, 3978–3988, doi:10.1175/2008JAS2613.1.

Crook, N. A., and D. F. Tucker, 2005: Flow over heated terrain. Part I: Linear theory and idealized numerical simulations. *Mon. Wea. Rev.*, **133**, 2552–2564, doi:10.1175/MWR2964.1.

Dai, A., and K. E. Trenberth, 2004: The diurnal cycle and its depiction in the Community Climate System Model. *J. Climate*, **17**, 930–951, doi:10.1175/1520-0442(2004)017<0930:TDCAID>2.0.CO;2.

Damiani, R., and Coauthors, 2008: The cumulus, photogrammetric, in situ, and Doppler observations experiment of 2006. *Bull. Amer. Meteor. Soc.*, **89**, 57–73, doi:10.1175/BAMS-89-1-57.

Deardorff, J. W., 1973: The use of subgrid transport equations in a three-dimensional model of atmospheric turbulence. *J. Fluids Eng.*, **95**, 429–438, doi:10.1115/1.3447047.

Done, J., C. A. Davis, and M. Weisman, 2004: The next generation of NWP: Explicit forecasts of convection using the Weather Research and Forecasting (WRF) model. *Atmos. Sci. Lett.*, **5**, 110–117, doi:10.1002/asl.72.

Egger, J., 1990: Thermally forced flows: Theory. *Atmospheric Processes over Complex Terrain, Meteor. Monogr.*, No. 23, Amer. Meteor. Soc., 43–57.

Emanuel, K. A., 1994: *Atmospheric Convection*. Oxford University Press, 592 pp.

Fuhrer, O., and C. Schär, 2007: Dynamics of orographically triggered banded convection in sheared moist orographic flows. *J. Atmos. Sci.*, **64**, 3542–3561, doi:10.1175/JAS4024.1.

Grabowski, W., and Coauthors, 2006: Daytime convective development over land: A model intercomparison based on LBA observations. *Quart. J. Roy. Meteor. Soc.*, **132**, 317–344, doi:10.1256/qj.04.147.

Heise, E., M. Lange, B. Ritter, and R. Schrodin, 2003: Improvement and validation of the multi-layer soil model. *COSMO Newsletter*, No. 3, COSMO, Deutscher Wetterdienst, Offenbach, Germany, 198–203.

Herzog, H.-J., G. Vogel, and U. Schubert, 2002: LLM—A nonhydrostatic model applied to high-resolving simulations of turbulent fluxes over heterogeneous terrain. *Theor. Appl. Climatol.*, **73**, 67–86, doi:10.1007/s00704-002-0694-4.

Hohenegger, C., P. Brockhaus, and C. Schär, 2008: Towards climate simulations at cloud-resolving scales. *Meteor. Z.*, **17**, 383–394, doi:10.1127/0941-2948/2008/0303.

——, L. Schlemmer, and L. Silvers, 2015: Coupling of convection and circulation at various resolutions. *Tellus*, **67A**, 26678, doi:10.3402/tellusa.v67.26678.

Houze, R., 1993: *Cloud Dynamics*. Academic, 573 pp.

Kain, J. S., and J. M. Fritsch, 1990: A one-dimensional entraining/detraining plume model and its application in convective parameterization. *J. Atmos. Sci.*, **47**, 2784–2802, doi:10.1175/1520-0469(1990)047<2784:AODEPM>2.0.CO;2.

Kendon, E. J., N. M. Roberts, C. A. Senior, and M. J. Roberts, 2012: Realism of rainfall in a very high-resolution regional climate model. *J. Climate*, **25**, 5791–5806, doi:10.1175/JCLI-D-11-00562.1.

Khairoutdinov, M., and D. Randall, 2006: High-resolution simulation of shallow-to-deep convection transition over land. *J. Atmos. Sci.*, **63**, 3421–3436, doi:10.1175/JAS3810.1.

Kirshbaum, D. J., 2011: Cloud-resolving simulations of deep convection over a heated mountain. *J. Atmos. Sci.*, **68**, 361–378, doi:10.1175/2010JAS3642.1.

——, and A. Grant, 2012: Invigoration of cumulus cloud fields by mesoscale ascent. *Quart. J. Roy. Meteor. Soc.*, **138**, 2136–2150, doi:10.1002/qj.1954.

——, G. H. Bryan, R. Rotunno, and D. R. Durran, 2007: The triggering of orographic rainbands by small-scale topography. *J. Atmos. Sci.*, **64**, 1530–1549, doi:10.1175/JAS3924.1.

Klemp, J. B., and R. B. Wilhelmson, 1978: The simulation of three-dimensional convective storm dynamics. *J. Atmos. Sci.*, **35**, 1070–1096, doi:10.1175/1520-0469(1978)035<1070:TSOTDC>2.0.CO;2.

Langhans, W., O. Fuhrer, and J. Schmidli, 2012a: Description and application of a budget-diagnosis tool in COSMO. *COSMO Newsletter*, No. 12, COSMO, Deutscher Wetterdienst, Offenbach, Germany, 43–51.

——, J. Schmidli, and C. Schär, 2012b: Bulk convergence of cloud-resolving simulations of moist convection over complex terrain. *J. Atmos. Sci.*, **69**, 2207–2228, doi:10.1175/JAS-D-11-0252.1.

——, ——, and B. Szintai, 2012c: A Smagorinsky-Lilly turbulence closure for COSMO-LES: Implementation and comparison to ARPS. *COSMO Newsletter*, No. 12, COSMO, Deutscher Wetterdienst, Offenbach, Germany, 20–31.

Lean, H. W., P. A. Clark, M. Dixon, N. M. Roberts, A. Fitch, R. Forbes, and C. Halliwell, 2008: Characteristics of high-resolution versions of the Met Office Unified Model for forecasting convection over the United Kingdom. *Mon. Wea. Rev.*, **136**, 3408–3424, doi:10.1175/2008MWR2332.1.

Leuenberger, D., M. Koller, O. Fuhrer, and C. Schär, 2010: A generalization of the SLEVE vertical coordinate. *Mon. Wea. Rev.*, **138**, 3683–3689, doi:10.1175/2010MWR3307.1.

Louis, J.-F., 1979: A parametric model of vertical eddy fluxes in the atmosphere. *Bound.-Layer Meteor.*, **17**, 187–202, doi:10.1007/BF00117978.

Lugauer, M., and P. Winkler, 2005: Thermal circulation in South Bavaria—Climatology and synoptic aspects. *Meteor. Z.*, **14**, 15–30, doi:10.1127/0941-2948/2005/0014-0015.

Mellor, G. L., and T. Yamada, 1974: A hierarchy of turbulence closure models for planetary boundary layers. *J. Atmos. Sci.*, **31**, 1791–1806, doi:10.1175/1520-0469(1974)031<1791:AHOTCM>2.0.CO;2.

——, and ——, 1982: Development of a turbulence closure model for geophysical fluid problems. *Rev. Geophys.*, **20**, 851–875, doi:10.1029/RG020i004p00851.

Orville, H. D., 1968: Ambient wind effects on the initiation and development of cumulus clouds over mountains. *J. Atmos. Sci.*, **25**, 385–403, doi:10.1175/1520-0469(1968)025<0385:AWEOTI>2.0.CO;2.

Petch, J., A. Brown, and M. Gray, 2002: The impact of horizontal resolution on the simulations of convective development over land. *Quart. J. Roy. Meteor. Soc.*, **128**, 2031–2044, doi:10.1256/003590002320603511.

Prein, A. F., and Coauthors, 2015: A review on regional convection-permitting climate modeling: Demonstrations, prospects, and challenges. *Rev. Geophys.*, **53**, 323–361, doi:10.1002/2014RG000475.

Raschendorfer, M., 2001: The new turbulence parameterization of LM. *COSMO Newsletter*, No. 1, COSMO, Deutscher Wetterdienst, Offenbach, Germany, 89–97.

Reinhardt, T., and A. Seifert, 2006: A three-category ice scheme for LMK. *COSMO Newsletter*, No. 6, COSMO, Deutscher Wetterdienst, Offenbach, Germany, 115–120.

Reiter, E. R., and M. Tang, 1984: Plateau effects on diurnal circulation patterns. *Mon. Wea. Rev.*, **112**, 638–651, doi:10.1175/1520-0493(1984)112<0638:PEODCP>2.0.CO;2.

Ritter, B., and J.-F. Geleyn, 1992: A comprehensive radiation scheme for numerical weather prediction models with potential applications in climate simulations. *Mon. Wea. Rev.*, **120**, 303–325, doi:10.1175/1520-0493(1992)120<0303:ACRSFN>2.0.CO;2.

Rockel, B., A. Will, and A. Hense, 2008: The regional climate model COSMO-CLM (CCLM). *Meteor. Z.*, **17**, 347–348, doi:10.1127/0941-2948/2008/0309.

Rotach, M. W., and D. Zardi, 2007: On the boundary-layer structure over highly complex terrain: Key findings from MAP. *Quart. J. Roy. Meteor. Soc.*, **133**, 937–948, doi:10.1002/qj.71.

Schär, C., D. Leuenberger, O. Fuhrer, D. Lüthi, and C. Girard, 2002: A new terrain-following vertical coordinate formulation for atmospheric prediction models. *Mon. Wea. Rev.*, **130**, 2459–2480, doi:10.1175/1520-0493(2002)130<2459:ANTFVC>2.0.CO;2.

Schlemmer, L., and C. Hohenegger, 2014: The formation of wider and deeper clouds as a result of cold-pool dynamics. *J. Atmos. Sci.*, **71**, 2842–2858, doi:10.1175/JAS-D-13-0170.1.

——, ——, J. Schmidli, C. S. Bretherton, and C. Schär, 2011: An idealized cloud-resolving framework for the study of midlatitude diurnal convection over land. *J. Atmos. Sci.*, **68**, 1041–1057, doi:10.1175/2010JAS3640.1.

Schmidli, J., 2013: Daytime heat transfer processes over mountainous terrain. *J. Atmos. Sci.*, **70**, 4041–4066, doi:10.1175/JAS-D-13-083.1.

——, and R. Rotunno, 2010: Mechanisms of along-valley winds and heat exchange over mountainous terrain. *J. Atmos. Sci.*, **67**, 3033–3047, doi:10.1175/2010JAS3473.1.

——, and ——, 2012: Influence of the valley surroundings on valley wind dynamics. *J. Atmos. Sci.*, **69**, 561–577, doi:10.1175/JAS-D-11-0129.1.

——, and Coauthors, 2011: Intercomparison of mesoscale model simulations of the daytime valley wind system. *Mon. Wea. Rev.*, **139**, 1389–1409, doi:10.1175/2010MWR3523.1.

Schwartz, C. S., and Coauthors, 2009: Next-day convection-allowing WRF model guidance: A second look at 2-km versus 4-km grid spacing. *Mon. Wea. Rev.*, **137**, 3351–3372, doi:10.1175/2009MWR2924.1.

Serafin, S., and D. Zardi, 2010: Daytime heat transfer processes related to slope flows and turbulent convection in an idealized mountain valley. *J. Atmos. Sci.*, **67**, 3739–3756, doi:10.1175/2010JAS3428.1.

Tiedtke, M., 1989: A comprehensive mass flux scheme for cumulus parameterization in large-scale models. *Mon. Wea. Rev.*, **117**, 1779–1800, doi:10.1175/1520-0493(1989)117<1779:ACMFSF>2.0.CO;2.

Wagner, A., 1932: Neue Theorie des Berg- und Talwindes (A new theory of mountain and valley winds). *Meteor. Z.*, **49**, 329–341.

Wagner, J. S., A. Gohm, and M. W. Rotach, 2014a: The impact of valley geometry on daytime thermally driven flows and vertical transport processes. *Quart. J. Roy. Meteor. Soc.*, **141**, 1780–1794, doi:10.1002/qj.2481.

——, ——, and ——, 2014b: The impact of horizontal model grid resolution on the boundary layer structure over an idealized valley. *Mon. Wea. Rev.*, **142**, 3446–3465, doi:10.1175/MWR-D-14-00002.1.

Weisman, M. L., W. C. Skamarock, and J. B. Klemp, 1997: The resolution dependence of explicitly modeled convective systems. *Mon. Wea. Rev.*, **125**, 527–548, doi:10.1175/1520-0493(1997)125<0527:TRDOEM>2.0.CO;2.

Whiteman, C. D., 1990: Observations of thermally developed wind systems in mountainous terrain. *Atmospheric Processes over Complex Terrain, Meteor. Monogr.*, No. 23, Amer. Meteor. Soc., 5–42.

Wicker, L. J., and W. C. Skamarock, 2002: Time-splitting methods for elastic models using forward time schemes. *Mon. Wea. Rev.*, **130**, 2088–2097, doi:10.1175/1520-0493(2002)130<2088:TSMFEM>2.0.CO;2.

Wulfmeyer, V., and Coauthors, 2011: The Convective and Orographically-Induced Precipitation Study (COPS): The scientific strategy, the field phase, and research highlights. *Quart. J. Roy. Meteor. Soc.*, **137**, 3–30, doi:10.1002/qj.752.

Wyngaard, J. C., 2004: Toward numerical modeling in the ''terra incognita.'' *J. Atmos. Sci.*, **61**, 1816–1826, doi:10.1175/1520-0469(2004)061<1816:TNMITT>2.0.CO;2.

Xu, K.-M., and Coauthors, 2002: An intercomparison of cloud-resolving models with the atmospheric radiation measurement summer 1997 intensive observation period data. *Quart. J. Roy. Meteor. Soc.*, **128**, 593–624, doi:10.1256/003590002321042117.